Int. J. Electrochem. Sci., 12 **(2017)** 8256 – 8268, doi: 10.20964/2017.09.26

International Journal of
ELECTROCHEMICAL
SCIENCE
www.electrochemsci.org

Insights into the $BaTiO_3$-Pb Perovskite Semiconducting Layer in PbO_2 Electrode Preparation by Electrochemical Deposition and Its Performance Evaluation

G. Muthuraman, K Kannan, and I.S. Moon[*]

Department of Chemical Engineering, Sunchon National University, 255-Jungang-ro, Suncheon-si, Jeollanam-do, 57922, South Korea
[*]E-mail: ismoon@sunchon.ac.kr

Received: 6 June 2017 / *Accepted:* 8 July 2017 / *Published:* 13 August 2017

PbO_2 electrode has high water splitting potential as that of BDD electrode, but no stability was shown in electrochemically deposited PbO_2 electrode. In this work, the effect of lower layer (a perovskite type dielectric $BaTiO_3$) on PbO_2 electrodeposition and its electrochemical performance evaluation was enrooted. $BaTiO_3$ was deposited on pretreated Ti in highly basic 4 M KOH medium resulted in needle shaped $BaTiO_3$ crystals of length 4.79 μm and width 0.43 μm. Co-deposition with nano-PbO_2 ($BaTiO_3$-NPb) and $Pb(NO_3)_2$ ($BaTiO_3$-Pb) produced a flower- and fur tree-like structures, respectively. Further, the upper layer of PbO_2 deposited in acid medium on $BaTiO_3$-NPb and $BaTiO_3$-Pb completely changed the shape to cauliflower-like shapes and cauliflower-like shapes with rock-like shapes, respectively. XRD result demonstrated the $BaTiO_3$ structure orientation was influenced to achieve mostly β-PbO_2 orientation. Electrochemical impedance and cyclic voltammetry analyses of $BaTiO_3$-NPb/PbO_2 and $BaTiO_3$-Pb/PbO_2 electrodes demonstrated smooth and porous morphological surfaces, respectively. When $BaTiO_3$-NPb/PbO_2 electrode was applied as an anode for the direct oxidation of phenol, it was found a considerable impact on its catalytic activity. An accelerated stability test result demonstrated $BaTiO_3$-NPb/PbO_2 is stable for more than 3000 h in H_2SO_4 medium.

Keywords: $BaTiO_3$, Morphological Change, Co-deposition, PbO_2.

1. INTRODUCTION

The exploration of anode materials with high surface area, catalytic activity, sustainability, and low cost is required for electrochemical applications such as the removal of pollutants and for the production of redox flow batteries [1,2]. In recent years, the development of bimetallic oxides has become of considerable importance due to their structural stabilities, which are highly related with structural reversibility, especially Li_2MnO_3 in lithium ion batteries as cathode [3]. Similarly, in

previous years, small constituents of Bi, Ag, Fe, in PbO_2 preparations have considerably increased its stability and catalytic activity [4-6], but the focus has been more on ceramic super lattices. The PbO_2 is still a potential anode material for many applications and has been much improved by the use of many constituents that enhance in fields, such as, pollutant degradation [7], the lead acid battery [8], and ferroelectric materials such as $PbTiO_3$ [9]. Conducting metals co-deposit with PbO_2 to produce rough porous surfaces, which in turn leads to the amplification in surface area and activity of the electrode [10]. Rajeshwar and co-workers incorporated nanometric TiO_2 particles into a cathodically deposited TiO_2 matrix in order to improve its photocatalytic and photoelectrochemical properties [11]. Many researchers have adopted the co-deposition, especially for PbO_2 preparation. Andersen et al., [12], and Musiani [13], repeatedly tested the co-deposition of PbO_2-matrix composites containing electrocatalytic oxides such as $Co3O_4$ [13-15] and RuO_2 [16,17] for oxygen evolution reactions (OER) via OH adsorption using different structural orientations. Perovskite-type (ABO_3) structured materials dominate the use of multilayer ceramic capacitors [18], chemical sensors, and nonvolatile memories [19], due to their attractive dielectric and ferroelectric characteristics [20]. Recently, a nanosized thin film $BaTiO_3$ electrode was used as a hydrogen peroxide sensor and found to have a low detection limit in a fast response time [21].

It is known that support materials has huge influence on the target material in structure related properties [3,22]. In solid oxide fuel cell (SOFC), YSZ ceramic coating under suitable sintering conditions on a NiO support found particle size distribution is a key factor [23,24]. An Au loaded rutile (TiO_2) has been found better photocatalyst than TiO_2 due to interfacial electron transfer from Au to TiO_2 [25]. In catalytic effect, a carbon support found good catalytic activity of PbO_2 on degradation of picric acid than the Pb support [26]. Aluminium base support found selective preparation of α-PbO_2 with strong adhesion properties [27]. In continuation of support material, perovskite type base materials found high stability and performance on PbO_2 [22]. Further, high breakdown voltage was found in $BaTiO_3$ by addition of MgO, which is more efficient in low voltage semi conducting purposes [28]. Also, the low layer oxide/upper layer oxide interaction could influence stability and catalytic activity. In fact, this interaction has been tested between layered Co and Ti oxides [29]. Moreover, the inert constituents such as perovskite generally makes stabilize the structure of the targeted material. With this aim, we have started to prepare PbO_2 on $BaTiO_3$ base material with different coating time and stability [30]. During the electrodeposition of $BaTiO_3$, we found difficulties like high voltage and plasma-like light generation. To avoid the high voltage, co-dopants were used in lower layer electrodeposition of $BaTiO_3$ that is become the main focus on the PbO_2 electrode preparation. This could help us understand the structure-function relationships that influence the stability and catalytic activity of PbO_2 electrode material.

In the present study, a perovskite-type $BaTiO_3$ deposited with co-dopant PbO_2 was prepared using a hydrothermal electro-deposition method using different conditions to form the lower layer. The upper layer PbO_2 was deposited electrochemically in acid medium. Morphological analyses SEM and XRD were conducted to find out the morphological effect of $BaTiO_3$-Pb on PbO_2. Interfacial properties were identified using electrochemical impedance spectroscopy (EIS) and cyclic voltammetry analyses. The stability and catalytic activity were evaluated for $BaTiO_3$-Pb/PbO_2 sandwich type electrode.

2. EXPERIMENTAL

2.1. Electrode Preconditioning and Experimental Conditions.

Titanium (Ti) mesh sheets 1 mm thick and 99.9% pure were purchased from Wesco (Korea). One centimeter square samples were mechanically polished using a metal brush and then degreased in acetone. Finally, degreased samples were dipped in 0.1 M HF (hydrofluoric acid) solution to remove oxides and metal impurities. The pretreated Ti was then used as anode and similar sizes graphite plates on both sides of the Ti anode (distance 0.5 cm) were used as cathodes. A 250-ml glass beaker was used as the electrolytic tank and was immersed in a temperature controlled water bath (HAAKE, Model-A81, Germany). Oxygen was continuously bubbled through the electrolyte. The electrolysis temperature was maintained at ca. 65 °C using a temperature controlled bath. The electrolyte, which contained 0.05 M $Ba(CH_3COO)_2$ (barium acetate) and 4 M KOH (potassium hydroxide), were prepared with Millipore (Human Corp. Model-Power III+, Korea) water to achieve a pH of 14 for preparation of barium titanate ($BaTiO_3$), either in the presence or absence of 1 wt % nano-PbO_2 ($BaTiO_3$-NPb) powder or 0.05 M $Pb(NO_3)_2$ ($BaTiO_3$-Pb). A similar experimental setup was used for PbO_2 deposition using 0.05 M of $Pb(NO_3)_2$ ($BaTiO_3$-NPb or Pb-PbO_2) in 0.1 M HNO_3 (nitric acid) medium.

2.2. Electrodeposition.

Electrolysis was performed using a DC power supply, BS 32C (0–100V, 0-50A), which was purchased from the Korea Switching Company in constant current mode (galvanostatic mode). Before electrolysis was started, the anode was initially immersed in the electrolyte nearly 1 min to condition its surface. $BaTiO_3$ deposition was performed in two steps as previous literature [31]. In brief, in a first step, a lower $BaTiO_3$ coating was formed on pretreated Ti sheet using a current density of 25 and 50 mA cm^{-2} for between 5 and 45 min. During $BaTiO_3$ deposition, the cell voltage was increased to 40 V and maintained. The $BaTiO_3$ deposit was dipped in hot ammonia treated water (pH 11) to minimize $BaCO_3$ formation, washed, rinsed in with Millipore water, and cleaned in ethanol using an ultrasonic cleaner for 1 min. PbO_2 was then deposited on the $BaTiO_3$ coating using a current density of 25 mA cm^{-2} for between 25 sec to 60 min in 0.1 M HNO_3 to form the upper layer. The cell voltage has increased to maximum of 15 V during the PbO_2 deposition.

2.3. Analysis.

Impedance measurements were obtained using a potentiostat (Princeton Applied Research, versaSTAT3, USA) using the frequency range between 100 kHz to 10 mHz with applied sine wave of 5 mV at OCP (open circuit potential) in 0.1 M Na_2SO_4 solution. Cyclic voltammetry (CV) cell was a three electrode cell with a working electrode, a platinum plate counter electrode and an Ag/AgCl (Satd. KCl) reference electrode. The electrochemically prepared electrode was served as working electrode. Scanning electron microscopy of the prepared PbO_2 electrodes was performed using a Zeiss EVO-

MA10 and film surface morphologies were investigated. XRD patterns of the as-prepared PbO_2 samples were obtained using a X'PERT-PRO X-ray diffractometer and Cu Kα radiation (λ=1.540598 À).

3. RESULTS AND DISCUSSION

3.1. Morphological analysis.

Fig. 1a and b show SEM images of electrodeposited $BaTiO_3$ and PbO_2 on a Ti substrate. A single step electrodeposition process was adopted to obtain nano size particles of $BaTiO_3$ and PbO_2. Temperature, current density, and time impacted the $BaTiO_3$ structure as previously reported by Srider et al., [31]. The selected conditions were 25 mA cm^{-2} for 30 min at 65°C, which produced a needle like structure with length of ~4.83 μm and diameter of ~0.43 μm (Fig. 1a). EDX data confirmed the presence of Ba with an atomic ratio of 18.19%, which supported the $BaTiO_3$ formation. Additionally, CV analysis (Fig.2 curve a) shows a redox peak between 130 to -60 mV, which resembled the formation of $BaTiO_3$, as reported previously [21], confirms the formation of $BaTiO_3$. In the case of PbO_2 electrodeposition on Ti, 25 mA cm^{-2} for 30 min at 65°C, where produced a sharp edged flower-like shapes (~0.2 μm) and hemispheric directionality (Fig. 1b). EDX analysis confirmed the presence of Pb with an atomic ratio of 26.95 %. Further, Pb presence was confirmed by CV analysis (Fig.2 curve b) in the form of PbO_2, which showed one oxidation peak and reduction peak at 1.51 and 0.91 V, respectively. These redox peaks well resembled with those previously reported for PbO_2 in 0.1 M PBS [32].

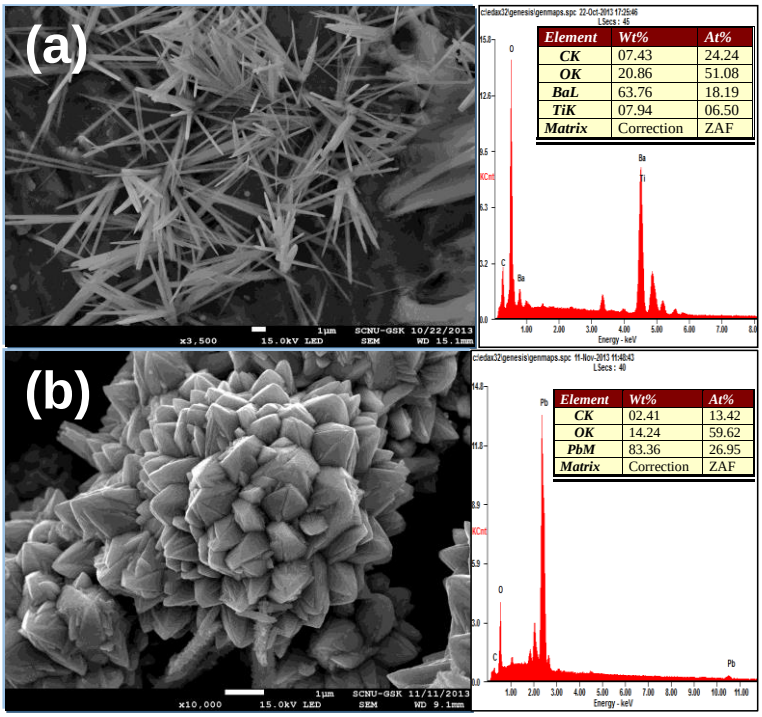

Figure 1. SEM images of $BaTiO_3$ deposited on Ti (a) and PbO_2 deposited on Ti (b) with their respective EDX data figure.

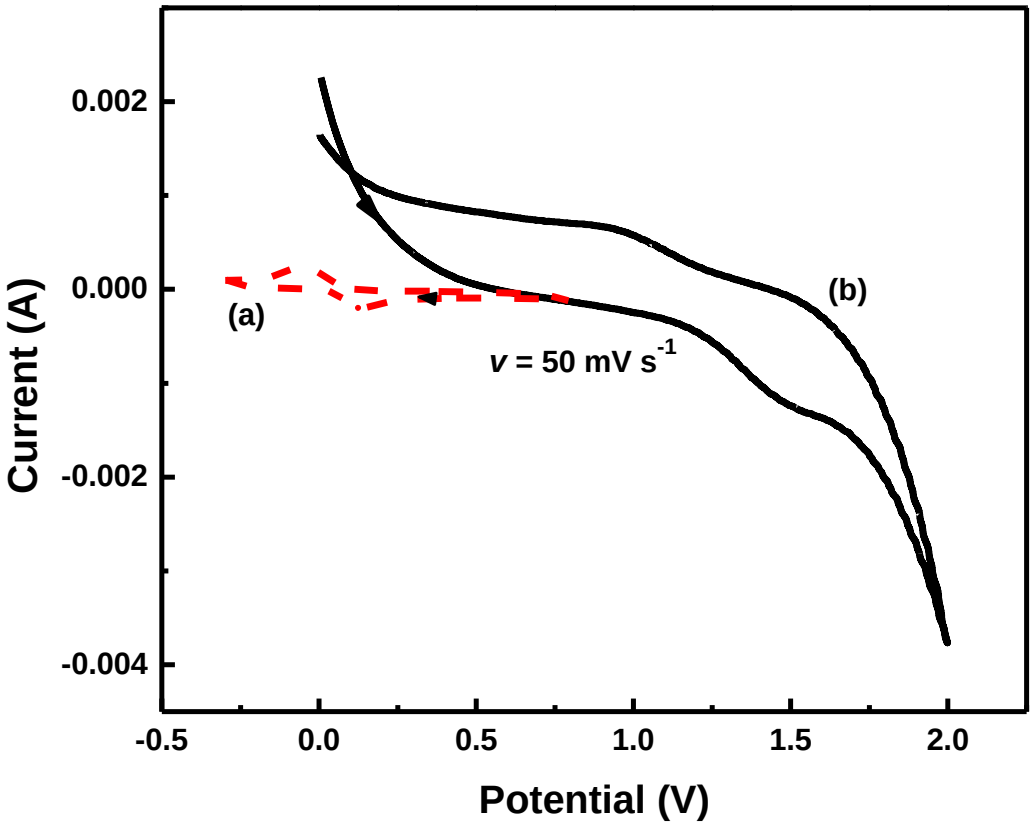

Figure 2. CV responses of (a) $BaTiO_3$; (b) PbO_2 in 0.1 M phosphate buffer solution (PBS) at a 50 mVs^{-1} scan rate. Electrodeposition was performed on Ti electrode in 4 M KOH at 65°C and a current density of 25 $mAcm^{-2}$ for 30 min.

As evidenced by the literature, stability and activity of TiO_2 have tremendously increased during co-deposition of metal or metal oxide along with primary compound deposition [11]. In consideration of $BaTiO_3$ electro-deposition in the lower layer on Ti, Pb ion insertion may enhance $BaTiO_3$ conductivity. When co-deposited, 1 wt% nano-PbO_2 powder or 0.05 M $Pb(NO_3)_2$ were used as co-dopant at 20 mA cm^{-2} for 30 min (nano-PbO_2) or 5 min ($Pb(NO_3)_2$) at 65°C, two different morphologies ~ 100 nm in size were obtained. Fig. 3a shows the cauliflower-like structure of nano-PbO_2 as co-dopant ($BaTiO_3$-NPb**)** and its associated EDX result confirmed the presence of Ba and Ti at atomic ratios of 2.91 and 3.22 %, respectively. One should be noted here that the obtained structure during co-deposition of nano-PbO_2 was completely unlike its sharp edged flower nature (Fig. 1b) and nano size particles (10 nm) appeared as the petals of a flower-like structure. Though 1wt % nano-PbO_2 used in 0.05M of $Ba(CH_3COO)_2$, PbO_2 dominated (81.36 wt %) but $BaTiO_3$ morphologically influenced electrode obtained. At the same time, co-deposition with $Pb(NO_3)_2$, to yields $BaTiO_3$-Pb (Fig. 3b), which had a fur tree like structure with Ba and Ti atomic ratios of 1.67% and 0.28%, respectively, by EDX, thus confirming the presence of $BaTiO_3$ and PbO_2. Pronounced morphological changes influenced by $BaTiO_3$ during the co-deposition of $Pb(NO_3)_2$ were observed even though the $BaTiO_3$ atomic ratio was much less than that of $BaTiO_3$-NPb(Fig. 3a).

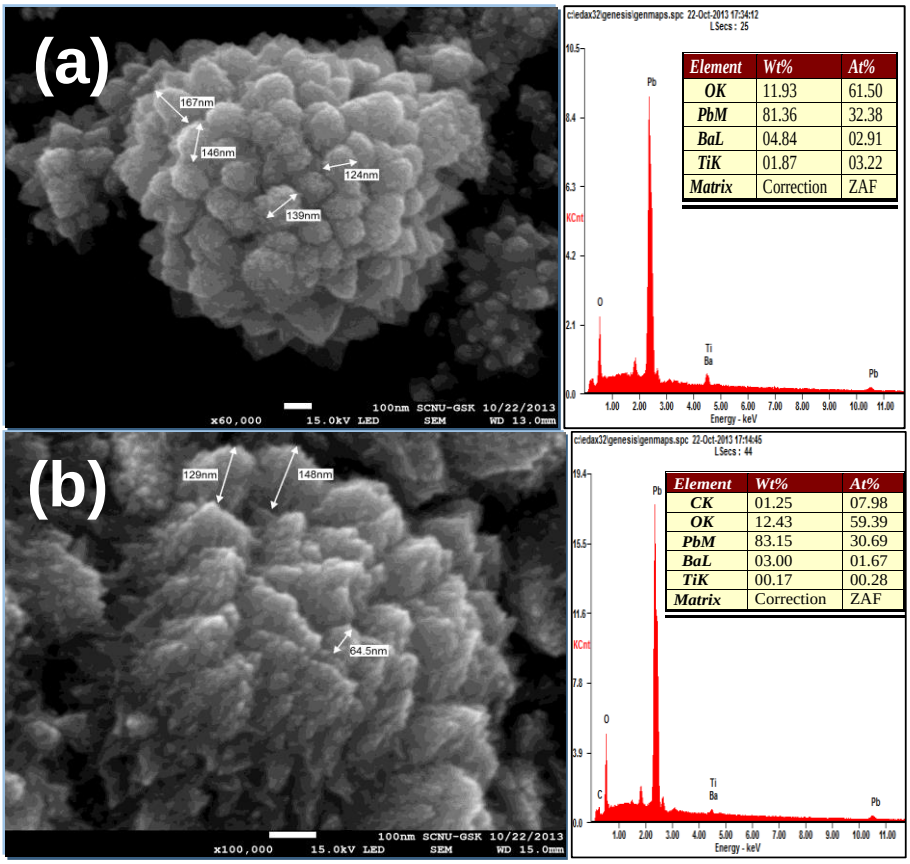

Figure 3. SEM images of lower layer $BaTiO_3$ co-deposited with nano-PbO_2 (a) and with $Pb(NO_3)_2$ (b) with their respective EDX data.

In consideration of upper layer deposition, β-PbO_2 is preferred due to its highly catalytic oriented structure [33]. The PbO_2 deposition was performed on both $BaTiO_3$-NPb and $BaTiO_3$-Pb surfaces using a current density of 25 mA cm^{-2} for 1 min in presence of 0.05 M $Pb(NO_3)_2$ in 0.1 M HNO_3 and 0.02 M HF (Fig. 4). A completely new morphological change from a fur tree-like to a cauliflower-like structure was obtained, after PbO_2 had been deposited on the $BaTiO_3$-Pb electrode surface. A black cloth-like layer was also observed to cover some areas between the cauliflower-like structures, which were very rich in K^+ ion according to EDX data (Fig. 4a).

This might have originated from KOH electrolyte during lower layer coating. The same EDX data also confirmed the near absence of Ti (atomic ratio 0.37) and absence of Ba, indicating that PbO_2 completely occupied on the first or lower layer of $BaTiO_3$-Pb. At the same time, PbO_2 deposition on $BaTiO_3$-NPb produced a cauliflower-like morphology with a stone-like structure of average size 3.2 μm. According to the EDX data of $BaTiO_3$-NPb (Fig. 4b), the stone-like morphology was enriched with 4.23 and 14.28 atomic % of Ba and Ti, respectively, indicating that the lower layer was still exposed at this given deposition conditions but that the $BaTiO_3$ morphology had been completely converted from its original needle like structure (Fig. 1b). Note that, the PbO_2 deposition has done by 25 sec to understand the structural change. $BaTiO_3$ morphological changes may have been due to the agglomeration of $BaTiO_3$ nano particles being solubilized by acid medium [34].

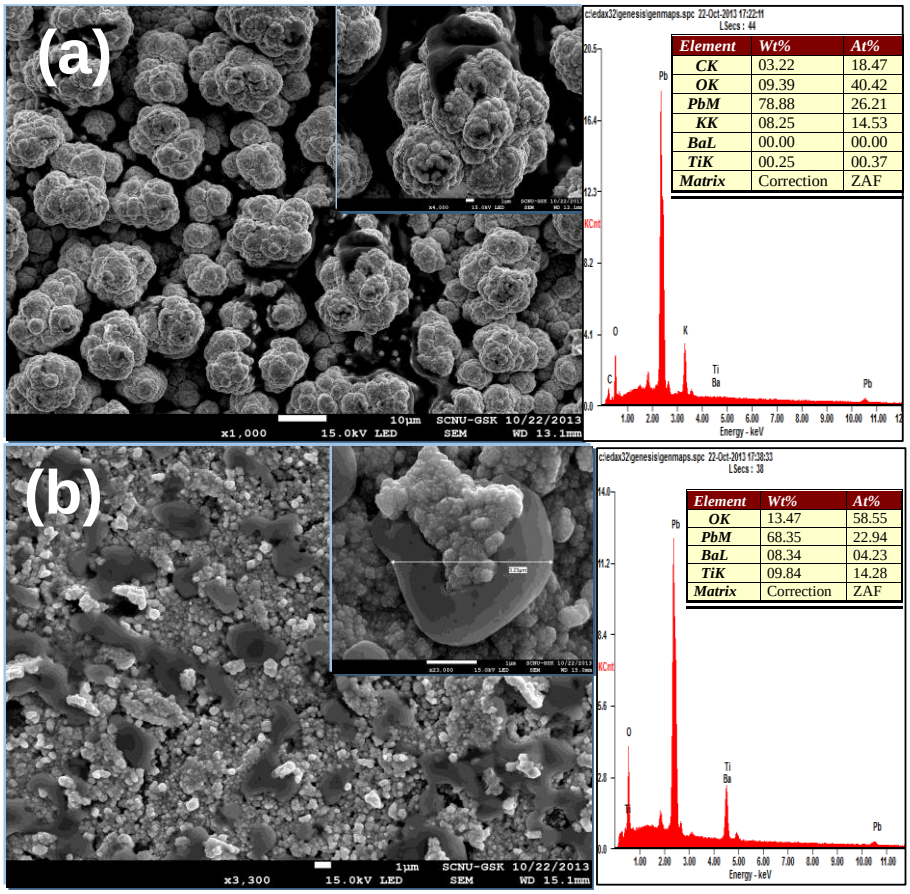

Figure 4. SEM images of upper layer β-PbO_2 deposited on $BaTiO_3$-NPb (a) and on $BaTiO_3$-Pb (b) with their respective EDX data.

X-ray diffraction patterns of $BaTiO_3$ and PbO_2 films on Ti prepared under different conditions using hydrothermal electro-deposition at 65°C are shown in Fig. 5. As-grown films were crystalline with micro/nano composites. A curve (a) in Fig. 5 indicates the presence of $BaTiO_3$ as predicted by peaks belonging to $BaTiO_3$, such as, 2θ = 21.98 (100), 31.36 (110), 38.64 (111), 44.93 (200), and 55.65 (112, 211) (VRC#98-002-8852). Furthermore, the existence of PbO_2 dominates during lower deposition of $BaTiO_3$ with co-deposition Pb using nano-PbO_2 ($BaTiO_3$-NPb, Fig. 5 curve (b)) and $BaTiO_3$ with co-deposition of Pb using $Pb(NO_3)_2$ ($BaTiO_3$-Pb Fig. 5 curve (c)). In case of the upper layer deposition of PbO_2, PbO_2/$BaTiO_3$-NPb (curve (d)) and PbO_2/$BaTiO_3$-Pb (curve (e)) shows PbO_2 dominated morphology. But, a broad peak at 2θ ~ 28 in Fig. 5(e) indicates still Ba exposure among the PbO_2 upper layer may be due to the agglomerated micro sized Ba in the lower layer (SEM and EDX data (Fig. 4b) might have hindered the formation of PbO_2 on the $BaTiO_3$. Remember that the deposition time of PbO_2 layer (second layer) has shorten purposely to understand the morphological phenomena between $BaTiO_3$ and PbO_2. In case of long time (60 min) PbO_2 deposition on the upper layer of $BaTiO_3$-NPb, the deposited electrode shows highly dominated peaks for only PbO_2 formation (VRC# 01-076-0564) as shown in Fig. 5(f). But a reduced peak intensity at 2θ value of ca. 28.49 plane found evident the α(111) plane [13] of PbO_2 becomes minimized, which means the β-PbO_2 formation

is predominant at this given condition. One can derive from XRD analyses that the first layer or lower layer of $BaTiO_3$ or co-deposited $BaTiO_3$ determines phase changes in upper layers.

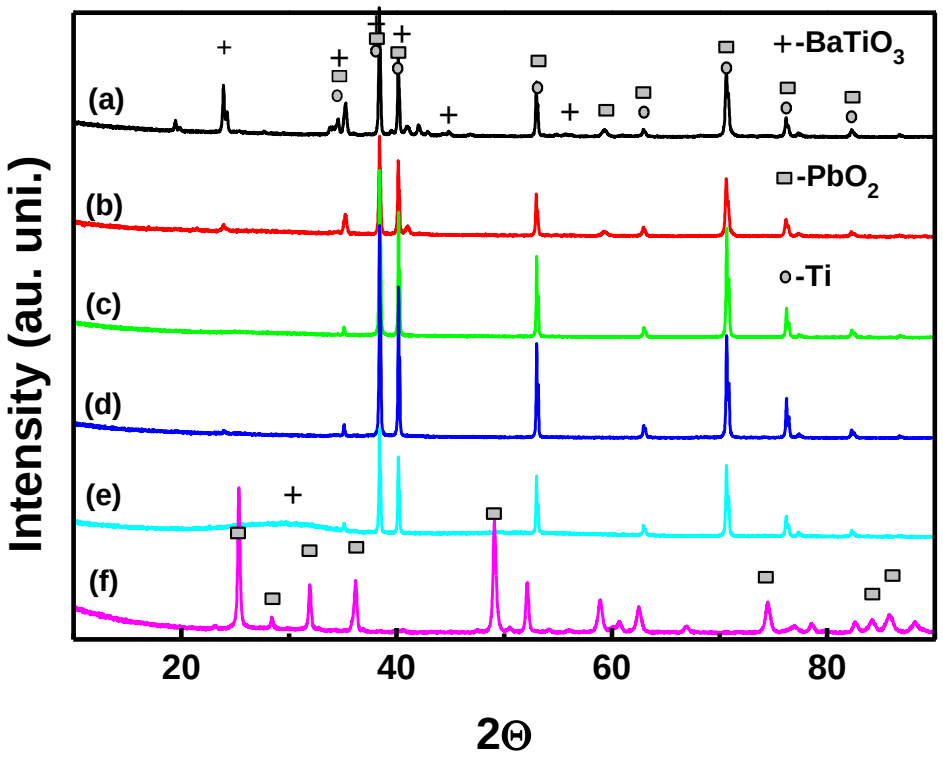

Figure 5. XRD patterns of as deposited $BaTiO_3$ (a), $BaTiO_3$-NPb (b), $BaTiO_3$-Pb (c), $BaTiO_3$-NPb/PbO_2 (d), and $BaTiO_3$-Pb/PbO_2 (e). PbO_2 deposition around 60 min on $BaTiO_3$-NPb (f).

3.2. Interfacial analysis.

Fig. 6 compares the Nyquist plots, of the impedances of $BaTiO_3$ and PbO_2, deposited on Ti electrodes in different combinations. Only the $BaTiO_3$ deposited electrode (Fig. 6A & B curve a) showed two straight lines, one at high frequency forming an angle of ~ 48° with the real axis and one less quasi-vertical at low frequency. Thus, the $BaTiO_3$ plot has the shape expected of a porous electrode and a well distributed pore size [35], which is in agreement with the SEM pictures of $BaTiO_3$ (Fig. 1a). In case of $BaTiO_3$-NPb electrode (Fig. 6A & B curve b), a depressed semicircle started from the higher to lower frequency region was observed, which explains the smooth, uniform surface [36] that in turn enhances conductivity. This surface phenomenon was well-matched by SEM morphology (Fig. 3a). A little straight line ~ 48° at the mid and lower frequency region with a deviated straight line ~30° at the higher frequency region makes $BaTiO_3$-Pb films (Fig. 6A & B curve c) a little porous (fur tree-like; Fig. 3b) with an uniform surface [36], alternatively, some loosely bound $Pb(NO_3)_2$ during deposition might have created some small pores. Upper layer deposition of PbO_2 on $BaTiO_3$-NPb (Fig. 6A & B curve d) produced a result similar to that observed for the $BaTiO_3$-NPb electrode with an extended semicircle in the mid and lower frequency regions, which indicates compact deposition with

minimized pores [36], though the $BaTiO_3$ agglomerated and became amorphous (Fig. 4b). For $BaTiO_3$-Pb/PbO_2 electrode (Fig. 6A & B curve e) showed almost a straight line ~ 45° at lower and middle frequencies with slight deviation from ~42° at higher frequencies resembling $BaTiO_3$-Pb but with an enhanced semicircle indicating a porous surface of loosely bound $Pb(NO_3)_2$ formed during deposition of lower layer was reflected by the upper layer [35].

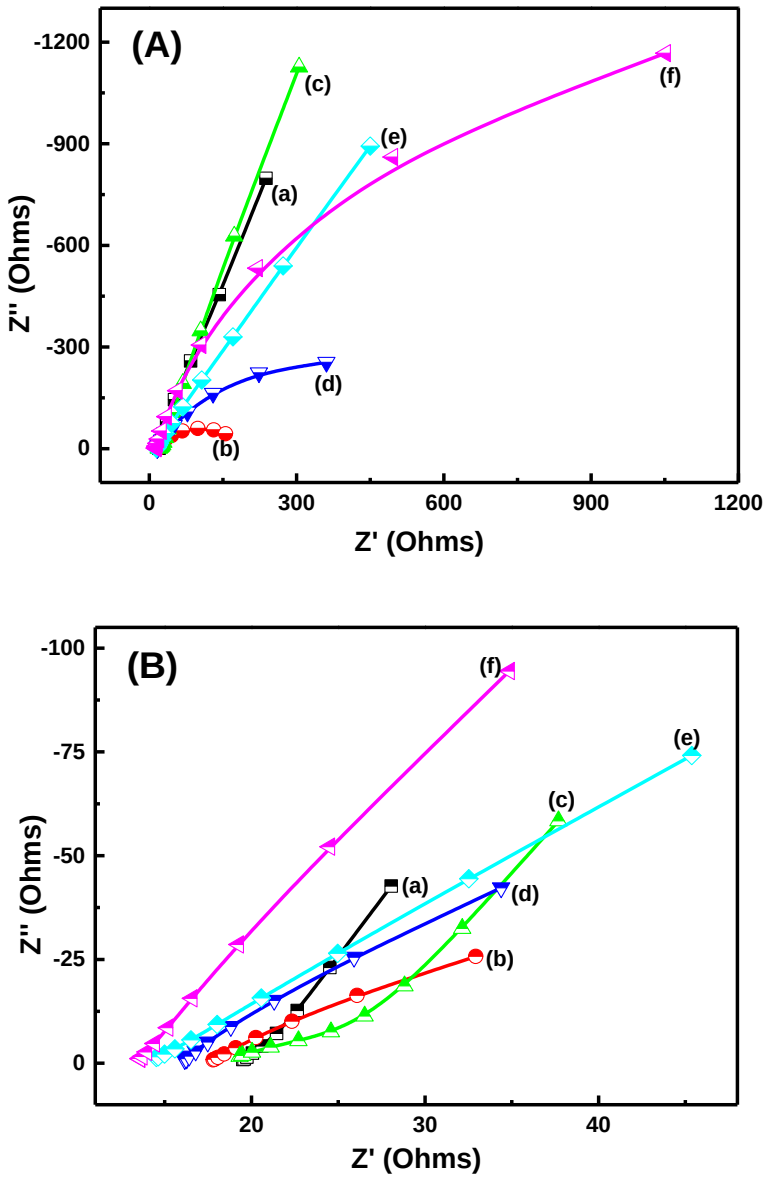

Figure 6. (A) Nyquist plots of the impedances of (a) $BaTiO_3$, (b) $BaTiO_3$-NPb, (c) $BaTiO_3$-Pb, (d) $BaTiO_3$-NPb/PbO_2, (e) $BaTiO_3$-Pb/PbO_2, and (f) layer by layer coating on $BaTiO_3$-NPb that operated in 0.1 M Na_2SO_4 solution under open circuit conditions. Deposition conditions: see experimental section and respective place in section 3.3. (B) Enlarged frequency figure of Fig. 6(A).

In the case of layer-by-layer coating of $BaTiO_3$-NPb and PbO_2 electrode (Fig. 6A & B curve f), shows a single big semi-circle with absence of another semicircle at high frequency region explains

compact film formation that depending on the lower layer impact [36]. In addition, there exist some differences between the ohmic resistances (high end frequency difference) of different PbO_2 thin films (Fig. 6B). The apparent ohmic or bulk solution resistance generated in the high frequency region at interface of PbO_2 thin films includes contributions from electrolyte resistance, contact resistance caused by the connection between $BaTiO_3$ and PbO_2, and pore resistance due to the porous structure of the films [35]. XRD results also corroborate SEM observations, interfacial activity depends on the lower layer structure, especially that of $BaTiO_3$ and precursor of co-dopant.

Also, the CV responses indicated interfacial activity based on redox behavior. The responses obtained for two different types of upper layer deposited $BaTiO_3$-NPb/PbO_2 and $BaTiO_3$-Pb/PbO_2 are depicted in Fig.7. For $BaTiO_3$-NPb/PbO_2, there appeared an ill-defined oxidation peak at 1.83 V in the forward scan, and two reduction peaks in the reverse scan at 0.92 V and 0.65 V, which are typical of PbO_2 oxidation and reduction behavior [32]. In the case of the $BaTiO_3$-Pb/PbO_2 electrode, a defined oxidation peak at 1.68 V in forward scan and two reduction peaks one at 0.95 V and another at 0.65 V appeared in the reverse scan. A 130 mV negative potential shift with a sharp oxidation peak for $BaTiO_3$-Pb/PbO_2 indicated the electrode was porous in nature [37]. At the same time, a positive potential shift with a non-defined oxidation peak for $BaTiO_3$-NPb is typical of a smooth morphology or slight ferroelectric $BaTiO_3$ exposure with a compact structure that needs a high activation energy for PbO_2 oxidation [37].

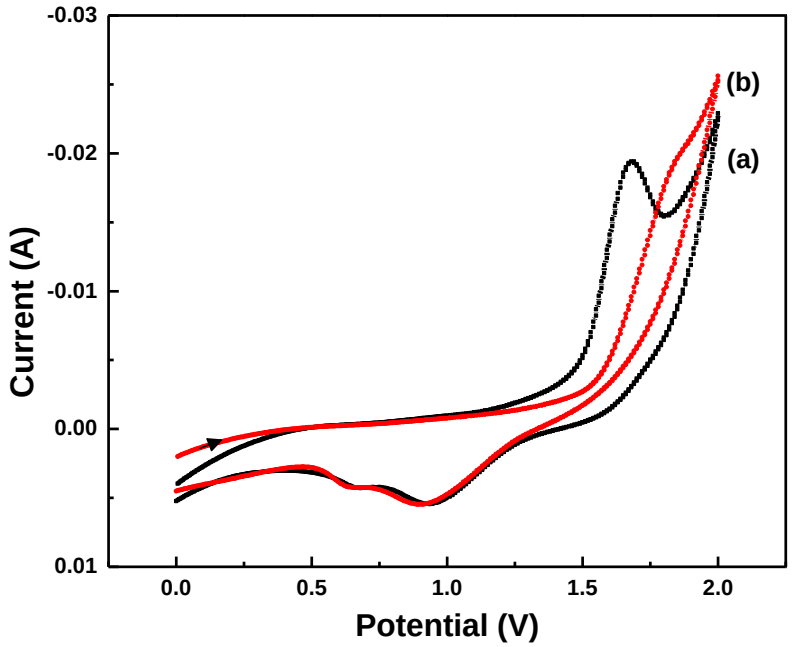

Figure 7. CV curves of as electrodes deposited in 0.1 M phosphate buffer solution (PBS) (a) $BaTiO_3$-NPb/PbO_2 and (b) $BaTiO_3$-Pb/PbO_2 at a scan rate of 50 mV s^{-1}.

3.3. Stability and Electrochemical applications.

It is evident from the literature that structural effects are highly influenced by the catalytic activity of the electrode, especially α- and β-PbO_2 electrodes [33], whereas the β-PbO_2 structure has a

more favorable catalytic effect due to its rutile structure. Fig. 8A shows the CV of a $BaTiO_3$-NPb/PbO_2 electrode in the presence and absence of 10 mM phenol in 0.1 M Na_2SO_4 solution.

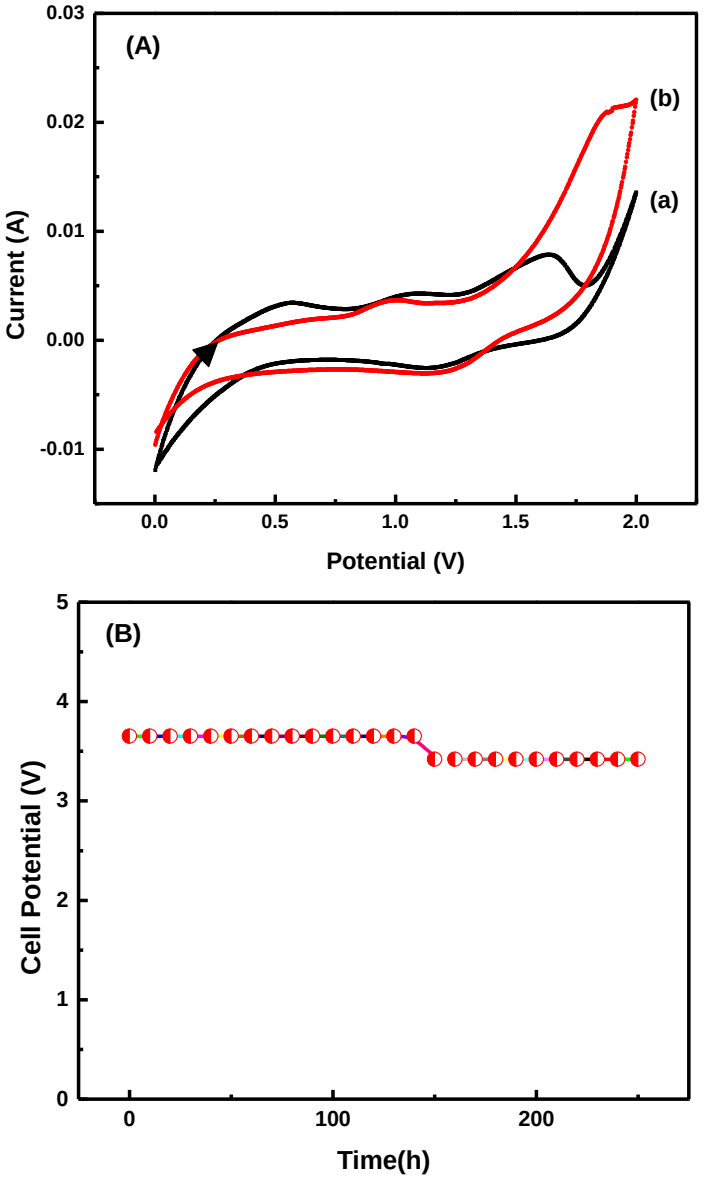

Figure 8. (A) CV results of the catalytic activity of the $BaTiO_3$-NPb/PbO_2 electrode in 0.1 Na_2SO_4 solution at a scan rate of 20 mV s^{-1}: (a) In the absence of 10 mM Phenol; (b) In the presence of 10 mM Phenol.

The CV response of the $BaTiO_3$-NPb/PbO_2 electrode in 0.1 M Na_2SO_4 showed two oxidation peaks, which is totally different from its CV response in 0.1 M PBS (Fig .7 curve a), at 1.03 V, and 1.65 V in forward scan, and these peaks were responsible for $Pb(SO_4)_2$ to PbO to PbO_2 oxidations [38]. In the reverse scan, one reduction peak was observed at 1.17 V, which was due to PbO_2 to $Pb(SO_4)_2$ conversion [38]. In the presence of 10 mM phenol, there appeared a huge increase in the oxidation peak in the PbO_2 oxidation potential region, which is typical electrochemical oxidation behavior (equation 1) [39].

$$BaTiO_3\text{-}NPb/PbO_2 + Phenol \longrightarrow BaTiO_3\text{-}NPb/Pb(SO_4)_2 + 2e^- + Product \quad ---(1)$$

In order to check the stability of the prepared electrode, a specially made 1 cm^2 mesh Ti electrode was treated and deposited as mentioned in the experimental section to produce a $BaTiO_3$-NPb/PbO_2 electrode with two additional layers by layer deposition. The prepared electrode was dipped in 1 M H_2SO_4 along with a Ti cathode of equal size. Electrolysis was started at an elevated current density of 300 mA cm^{-2}, which was 12 times higher than that used for normal electrolysis (25 mA cm^{-2}) [40]. Fig. 8B shows the initial cell potential 3.65 V, which was maintained for up to 140 h, reduced to reach 3.42 V at 250 h, and then remained constant. This 200 mV difference over 250 h is considered almost no change in potential indicates no change in the electrode morphology. The approximate total stability duration was calculated to be 3000 h (250 h x 12) at an applied current density of 25 mA cm^{-2}, which meets the requirements of industrial application.

(B) Cell potential variations with time in the stability test of the $BaTiO_3$-NPb/PbO_2 electrode in 1 M H_2SO_4 solution.

4. CONCLUSIONS

We investigated the influence of perovskite type $BaTiO_3$ on PbO_2 electrode preparation in terms of morphological insights towards catalytic activity and stability for the first time. Depending upon the co-dopants nano-PbO_2 and $Pb(NO_3)_2$, the lower layer of $BaTiO_3$ morphology was found smooth and porous, respectively. The upper layer of PbO_2 on $BaTiO_3$-NPb or $BaTiO_3$-Pb exhibits high structural control due to its perovskite ceramic nature. The found high catalytic and stability of $BaTiO_3$ NPb/PbO_2 confirms strong influence on upper PbO_2 layer, which can be further improved by controlling $BaTiO_3$-NPb and PbO_2 layer thickness. The developed electrode is scheduled to be tested and optimized in a mediated electrochemical oxidation system for practical application.

ACKNOWLEDGEMENTS

This work was supported by the National Research Foundation (NRF) funded by Ministry of Engineering Science and Technology (MEST) from the Korean government (Grant No. NRF-2017R1A2A1A05001484).

References

1. M. Zhou, Q. Dai, L. Lei, C.A. Ma, D. Wang, M. Zhou, Q. Dai, L. Lei, C.a. Ma, D. Wang, *Environ. Sci. Technol.* 39 (2005) 363-370.
2. D. Pletcher, F. C. Walsh, Industrial Electrochemistry, Chapman and Hall, London, 1990.
3. C. Zhao, X. Wang, X. Liu, H. Zhang, Q. Shen, *ACS Appl. Mater. Interfaces* 6 (2014) 2386-2392.
4. J. Ge, D.C. Johnson, *J. Electrochem. Soc.* 142 (1995) 1525-1531.
5. J. Feng, D.C. Johnson, *J. Electrochem. Soc*. 137 (1990) 507-510.
6. I.H. Yeo, S. Kim, R. Jacobson, D.C. Johnson, *J. Electrochem. Soc*. 136 (1989) 1395-1401.

7. L.S. Andrade, R.C. Rocha-Filho, N. Bocchi, S.R. Biaggio, J. Iniesta, V. Garcia-Garcia, V. Montiel, *J. Hazard. Mater*. 153 (2008) 252-260.
8. J. Collins, X. Li, D. Pletcher, R. Tangirala, D. Stratton-Campbell, F.C. Walsh, C. Zhang, *J. Power Sources* 195 (2010) 2975-2978.
9. J.F. Scott, C.A. Paz de Araujo, *Science* 246 (1989) 1400-1405.
10. A.R. Despic´, A. R.; K.I. Popov, K. I. In Modern Aspects of Electrochemistry; Conway, B. E., Bockris, J. O'. M., Eds.; Plenum Press: New York, 1972; Vol. 7, p. 199.
11. C.R. Chenthamarakshan, N.R. de Tacconi, K. Rajeshwar, R. Shiratsuchi, *Electrochem. Commun*. 4 (2002) 871-876.
12. T.N. Andersen, C.H. Pitt, L.S. Livingston, *J. Appl. Electrochem*. 13 (1983) 429-438.
13. M. Musiani, , *Chem. Commun*. (1996) 2403-2404.
14. R. Bertoncello, F. Furlanetto, P. Guerriero, M. Musiani, *Electrochim. Acta* 44 (1999) 4061-4068.
15. S. Cattarin, P. Guerriero, M. Musiani, *Electrochim. Acta* 46 (2001) 4229-4234.
16. M. Musiani, F. Furlanetto, R. Bertoncello, *J. Electroanal. Chem*. 465 (1999) 160-167.
17. R. Bertoncello, S. Cattarin, I. Frateur, M. Musiani, *J. Electroanal. Chem*. 492 (2000) 145-149.
18. S. Ghosh, S. Dasgupta, A. Sen, H.S. Maiti, *Mater. Lett*. 61 (2007) 538-541.
19. S. Venigalla, *Am. Ceram. Soc. Bull*. 79 (2000) 47-48.
20. K. Yamada, S. Kohiki, *Physica* E: 4 (1999) 228-230.
21. X. He, C. Hu, Y. Xi, B. Wan, C. Xia, *Sensor. Actuat. B-Chem*. 137 (2009) 62-66.
22. H. An, Q. Li, D. Tao, H. Cui, X. Xu, L. Ding, L. Sun, J. Zhai, *Appl. Surf. Sci*. 258 (2011) 218-224.
23. L. Lu, C. Ni, M. Cassidy, J.T.S. Irvine, *J. Mater. Chem.* A (2016), DOI: 10.1039/C6TA04074H.
24. E. Olevsky, T.T. Molla, H.L. Frandsen, R. Bjørk, V. Esposito, D.W. Ni, A. Ilyina, N. Pryds, *J. Am. Ceram. Soc.* 96 (2013) 2657-2665.
25. C.K. Song, J. Baek, T.Y. Kim, S. Yu, J.W. Han, J. Yi, *Appl. Catal*., B 198 (2016) 91-99.
26. G.N. Abu, H. Tamos, S.H. Abu, A.M. El, A.A.R. El, *Global J. Environ. Sci. Technol*., 2 (2012) 12-19.
27. B.-M. Chen, Z.-C. Guo, X.-W. Yang, Y.-D. Cao, *J. Nonferr. Metal. Soc*. 20 (2010) 97-103.
28. T.E. Murphy, D. Chen, J.D. Phillips, *Appl. Phys. Lett*., 85 (2004) 3208-3210.
29. Y. Shao, W. Chen, E. Wold, J. Paul, *Langmuir* 10 (1994) 178-187.
30. G. Muthuraman, K. Karunakaran, I. S. Moon, *Mater. Technol*. 50(2) (2016) 211-215
31. S. Venigalla, R.E. Chodelka, J.H. Adair, *J. Am. Ceram. Soc*. 81 (1998) 2429-2442.
32. M.E. Hyde, R.M.J. Jacobs, R.G. Compton, *J. Phys. Chem*. B 108 (2004) 6381-6390.
33. P.N. Bartlett, T. Dunford, M.A. Ghanem, *J. Mater. Chem*. 12 (2002) 3130-3135.
34. J.P. Remeika, W.M. Jackson, *J. Am. Chem. Soc*. 76 (1954) 940-941.
35. C.V. D'Alkaine, P. Mengarda, P.R. Impinnisi, *J. Power Sources* 191 (2009) 28-35.
36. T. Chen, H. Huang, H. Ma, D. Kong, *Electrochim. Acta*, 88 (2013) 79-85.
37. Z.-D. Huang, X.-M. Liu, S.-W. Oh, B. Zhang, P.-C. Ma, J.-K. Kim, *J. Mater. Chem*., 21 (2011) 10777-10784.
38. D. Zhou, L. Gao, *Electrochimica Acta* 53 (2007) 2060-2064.
39. A.J. Bard, L.R. Faulkner, Electrochemical Methods: Fundamentals and Applications, Wiley–Interscience, New York, 1980.
40. C.A. Martínez-Huitle, M.A. Quiroz, C. Comninellis, S. Ferro, A.D. Battisti, *Electrochim. Acta* 50 (2004) 949-956.